Coupled thermal transport and mass diffusion during vapor absorption into hygroscopic liquid desiccant droplets

Coupled thermal transport and mass diffusion during vapor absorption into hygroscopic liquid desiccant droplets

Zhenying Wang[a,b,†], Daniel Orejon[a,b], Khellil Sefiane[c,a], Yasuyuki Takata[a,b,‡]

a International Institute for Carbon-Neutral Energy Research (WPI-I^{2}CNER), Kyushu University, Fukuoka 819-0395, JP

b Thermofluid Physics Laboratory, Department of Mechanical Engineering, Kyushu University, Fukuoka 819-0395, JP

c Institute of Multiscale Thermofluid, School of Engineering, University of Edinburgh, King's Buildings, Edinburgh EH9 3JL, UK

Corresponding author: † z.wang@heat.mech.kyushu-u.ac.jp; ‡ takata@mech.kyushu-u.ac.jp.

Tel: (+81) 092-802-3133; (+81)092-802-3100.

ABSTRACT

Phase change phenomena at a droplet scale have gained extensive attention in recent years due to the unique aspects that can be exploited in a wide range of domestic and industrial applications. Different from existing studies on droplet evaporation and/or dropwise condensation, this work focuses on the mechanisms of vapor absorption into hygroscopic liquid desiccant droplets, which are of interest to many dehumidification and absorption processes. In particular we investigate the coupled heat and mass transport during vapor absorption into single droplets using optical imaging and infrared thermography. Driven by the vapor pressure difference between the ambient and the droplet surface, desiccant droplets grow due to water uptake. The droplet growth rate and final expansion ratio depend on the ambient temperature and relative humidity. After liquid desiccant droplet deposition onto the substrate, and as a consequence of the initial fast vapor absorption, droplets experience an increase in temperature. They then gradually cool down as a result of heat dissipation into the substrate and into the ambient combined with the decrease in the vapor absorption rate, *i.e.*, heat of absorption. The temperature rise measured by infrared thermography is confirmed by the calculation of the heat of absorption for six representative environmental conditions. Furthermore the vapor pressure at the

droplet surface is estimated by combining the changes of interfacial temperature and salt concentration within the droplet bulk. As water absorbs into the droplets, the salt concentration decreases and so does the driving force for vapor diffusion and hence the heat of absorption. As a contrast, experiments with evaporating water droplets show different evolution of droplet profile, different dynamics of the triple contact line, as well as the occurrence of evaporative cooling. We conclude on the importance of taking account of the coupling mechanisms of absorptive heating and volume growth during vapor absorption into liquid desiccant droplets. Findings presented here provide a valuable extension to existing literature of phase change at the droplet scale, which contributes to a more complete understanding of the role of liquid desiccant droplets in dehumidification processes.

Keywords: vapor absorption, liquid desiccant, droplet evaporation, heat transport, mass diffusion

1. INTRODUCTION

Liquid desiccant is a type of aqueous salt solution characterized by its excellent hygroscopic properties [1] widely used in dehumidification [2] and absorption systems [3-5]. By taking advantage of the vapor absorption capability of liquid desiccants, further optimization of indoor environment control, energy conservation, and emission reduction, has been pursued. In the abovementioned practical systems, the heat and mass transfer between liquid desiccant and humid air (or water vapor) is paramount. This has gained increasing attention from researchers in the field of energy system design and optimization. Nevertheless, despite the numerous existing studies on dehumidification devices mainly carried out at the macroscale [6-9], the behavior of single liquid desiccant droplets in contact with humid air has been scarcely reported.

Up to now, existing studies on the phase change phenomena at the droplet scale mainly focus on

droplet evaporation [10-14] and on dropwise condensation [15-17]. Different from single-component droplets, liquid desiccant is a mixture of water and desiccant salt. The different composition of liquid desiccant droplets provides unique hygroscopic properties that differ from those of pure liquid droplets. Along with vapor absorption or desorption, the solute concentration within the droplet changes, which in turn influences the solute diffusion and the phase transition at the droplet surface.

Regarding aqueous salt solution droplets, research mainly focuses on the evaporation behavior and on the crystalline deposits from drying droplets due to water loss. Soulie et, al. [18] investigated the behavior of aqueous saline-water ($NaCl$-H_2O) solution droplets with various salt concentrations. They concluded on the strong effects of salt concentration on both contact line pinning and evaporation rate. Brenn [19] simulated the concentration distribution within aqueous salt solution droplets during evaporation. Larger concentration gradient, function of the radial coordinate, is reported at high evaporation rate. Misyura [20-22] carried out experiments with aqueous salt solution droplets on smooth and structured heated surfaces, and provided detailed analyses of the heat transfer within the liquid layer and on the effect of crystallization on the evaporation rate. Zhong et, al. [23] studied the effect of surface wettability on the evaporation of sessile saline droplets. Results demonstrate the dependence of contact line dynamics and crystalline morphology on salt concentration and surface wettability. Other influencing factors on the evaporation behavior and on the crystal patterns formed from the dry-out of saline droplets have been presented by McBride [24], Shahidzadeh-Bonn [25], Kaya [26], Harrington et al. [27]. The reader is also referred to the review papers of Sefiane and Parsa *et al.* [28, 29].

The studies reported above confirmed the strong effects of non-evaporative salt ions present in the

66 droplet on the evaporation process. For aqueous solution droplets, the vapor pressure at the droplet
67 surface is lower due to the existence of non-evaporating salt ions, and therefore a heated surface is
68 usually required to assist droplet evaporation. Moreover, the evaporation rate depends on the type of
69 dissolved salt. As revealed by Misyura's experiments [30], the evaporation rates of NaCl, CsCl, and
70 $BaCl_2$ salt solutions are virtually constant throughout the complete evaporation process, whereas the
71 evaporation rates of LiBr, LiCl, $CaCl_2$, $MgCl_2$ liquid desiccant salt solutions decrease as a consequence
72 of the increase in salt concentration as water evaporates. Compared to ordinary salts such as NaCl,
73 desiccant salts (LiBr, LiCl, $CaCl_2$, $MgCl_2$) have much higher adhesion force to water molecules,
74 therefore, the vapor pressure at the droplet surface is strongly function of the salt concentration.
75 Recently, Wang *et al.* reported on the mechanisms of growth and spreading of hygroscopic lithium-
76 bromide droplets during water vapor absorption, initiating a new avenue for the study of the
77 fundamentals of vapor absorption into liquid desiccant droplets [31]. The mentioned work mainly
78 focuses on the effects of substrate wettability on the vapor absorption rate and on the droplet dynamics.
79 An unexpected droplet spreading on hydrophilic glass substrates is observed and explained by
80 theoretical analyses. This work, on the other hand, focuses on the thermal transport and mass diffusion
81 process during vapor absorption. At ordinary ambient conditions and without additional substrate
82 heating, the vapor pressure at the surface of a liquid desiccant droplet becomes lower than the partial
83 vapor pressure of the ambient. Driven by the vapor pressure difference between the ambient and the
84 droplet surface, water vapor diffuses from the ambient towards the droplet interface. Then water gets
85 absorbed into the droplet bulk, and the droplet volume increases. Along with the vapor-liquid phase
86 change at the droplet surface, heat of absorption is released causing a temperature increase at the

droplet surface. Then, because of the induced temperature gradient, heat transfer between the droplet and its surroundings takes place. The temperature change also influences the vapor pressure at the droplet surface, which subsequently affects the vapor diffusion on the air side. The strong coupling of heat and mass transfer mechanisms in single liquid desiccant droplets shows the interesting and complex phenomena taking place during vapor absorption at the droplet scale. A better understanding of the coupling mechanisms of heat and mass transfer during vapor absorption is of significance to basic science and can be utilized for a better design of the initial stage in dehumidification processes.

Consequently, in this study, we investigate the heat and mass transport coupling mechanisms during vapor absorption into lithium bromide desiccant (LiBr-H_2O) droplets in controlled environmental conditions. The evolution of droplet profile and the temperature distribution at the droplet surface are investigated using optical imaging and infrared (IR) thermography. In addition, experimental observations of droplet growth during absorption into liquid desiccant droplets are compared to those of water droplet evaporation. In the case of water droplets, the effect of evaporative cooling causes a temperature decrease at the droplet interface, and subsequently affects the evaporation rate. Whereas in the case of liquid desiccant droplets, both the salt concentration and temperature at the droplet interface will change due to water uptake and due to the heat released during phase transition. The local change of the salt concentration and temperature at the droplet interface in turn affects the driving force for vapor diffusion on the air side. Further analyses are carried out to quantitatively explain the heat and mass transfer mechanisms underlying the reported phenomena. We conclude on the need for an accurate account of the coupled heat and mass transfer mechanisms in order to provide a complete description of the vapor absorption process into liquid desiccant droplets,

which is of great importance for the accurate design of the initial stage for dehumidification processes.

2. EXPERIMENTAL METHODS

Experimental setup: Experiments are conducted within an environmental chamber with accurately controlled conditions (800L, -20 °C ~ 100 °C, 20% ~ 98% *RH*, PR-3KT from ESPEC Corp.). The accuracy of environmental temperature is ± 0.5 °C, while that of relative humidity is ± 5% *RH*. Figure 1(a) shows the experimental setup used in this study. Six representative experimental conditions are chosen with ambient temperature of 25 °C, 45 °C, and relative humidity of 30% *RH*, 60% *RH*, 90% *RH* (presented in Figure 2(a)). During experiments, the evolution of the droplet profile is recorded with a high-definition CCD camera (Sentech STC-MC152USB with a RICOH lens and 25-mm spacing ring) at 4.8 frames per second, and an LED backlight is applied to enhance the image contrast. The recorded video of the droplet profile is then processed with MATLAB® and ImageJ® to extract the evolution of contact radius, R (mm), and contact angle, θ (deg), of the droplet with time, t (seconds). Figure 1(b) includes a typical snapshot of the droplet profile used to extract the droplet contact radius, contact angle, and height. Further details regarding the experimental setup and procedure abovementioned can be found in Ref. 31 [31]. Additionally, to be able to address the heat transport problem, an IR camera, FLIR SC-4000 with a spectral range between 3.0 and 5.0 μm and a resolution of 18 mK, is setup vertically looking at the substrate from the top. Thermal evolution at the droplet liquid-gas interface is recorded at 2 frames per second. The influence of ambient condition on the transmissivity of the air (different ambient temperature and different *RH*) between the droplet surface and the IR camera lens is corrected depending on the experimental conditions using the ThermCam Researcher PRO 2.10 software from FLIR.

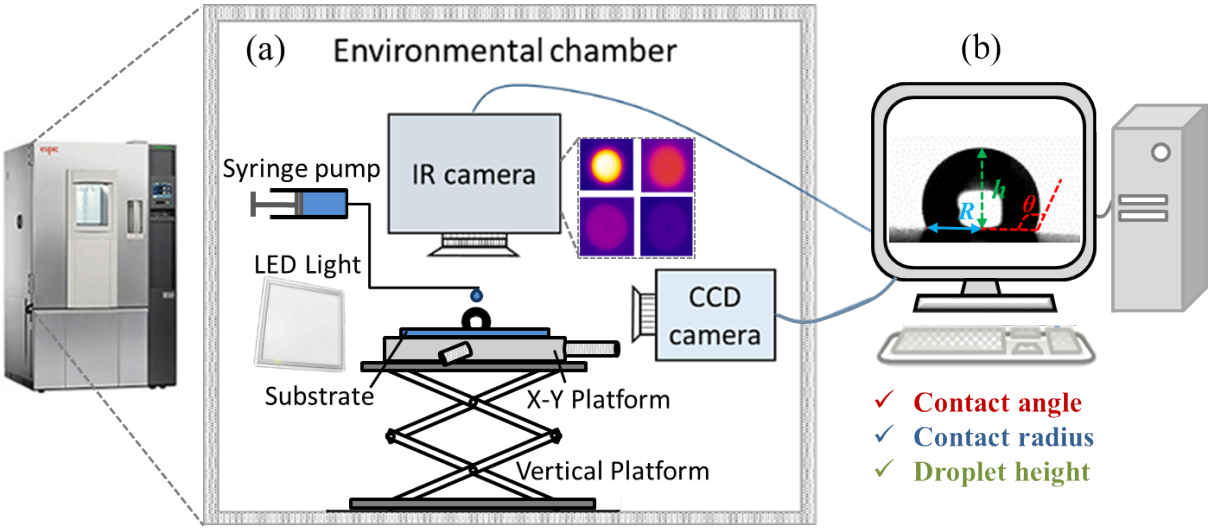

Figure 1 Overview of the experimental setup. (a) Experimental setup: environmental chamber, CCD camera, IR camera, back light, stainless steel vertical platform, x-y platform, droplet dosing system; (b) Data acquisition system with ImageJ® and Matlab®.

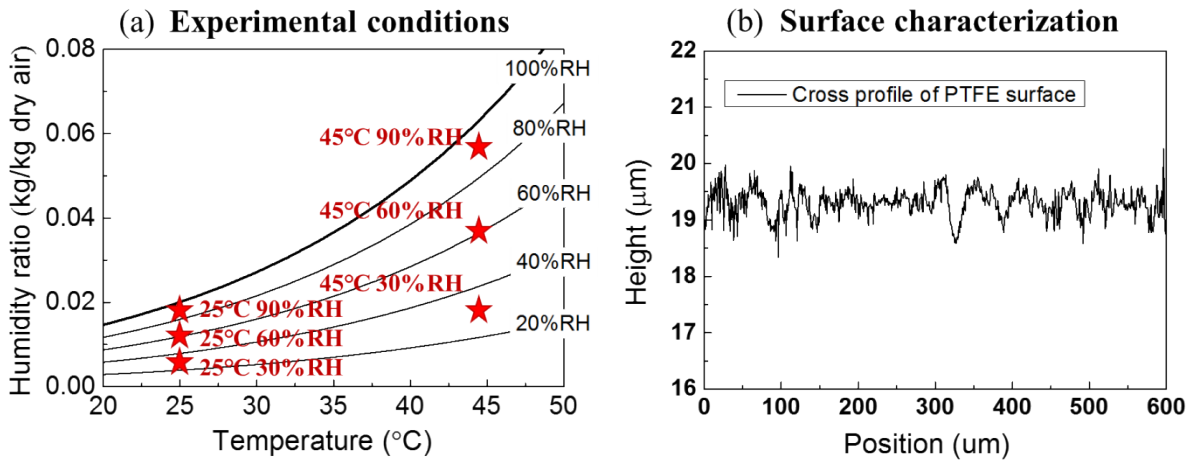

Figure 2 Environmental conditions and surface characterization: (a) Experimental temperature and relative humidity shown on the psychrometric chart; (b) Cross profile of PTFE surface characterized by Olympus LEXT OLS4000.

Materials and preparation: Lithium bromide-water (LiBr-H_2O) solution with a mass fraction of 54 wt.% from Sigma-Aldrich is used as the testing fluid for vapor absorption experiments. For the sake of comparison, contrast experiments of droplet evaporation are conducted using distilled water (Sigma-Aldrich). The physical properties of the two fluids at 20 °C and at 1 atmosphere are given in Table 1. Smooth polytetrafluoroethylene (PTFE), which is a commonly used material in dehumidification

142 systems, is investigated as the testing substrate. The representative cross profile of the PTFE surface
143 is shown in Figure 2(b), which is characterized with a confocal laser scanning microscope (Olympus
144 LEXT OLS4000, Japan). The thermophysical properties of PTFE are listed in Table 2. Before
145 experiments, substrates are cleaned by immersing each sample in an ultrasonic bath with ethanol for
146 15 minutes. After that, the sample is taken out and flushed with large amount of deionized water. Then,
147 substrates are further dried with filtered compressed air to remove any possible remaining dust or
148 contaminants. After cleaning, the substrate is placed inside the chamber for sufficiently long time for
149 the substrate and the environment to reach equilibrium. Then, a droplet with a controlled volume of
150 3.2 ± 0.3 microliters is deposited on the PTFE substrate. We note here that the contact radius of both
151 pure water and LiBr-H_2O droplets lies below the capillary length scale ($\lambda = \sqrt{\gamma_{lg}/\rho g}$ [32]), which is
152 *ca.* 2.7 mm for water and *ca.* 2.42 mm for 54 wt.% LiBr- H_2O in air at 20 °C. Thus, the gravity effect
153 on the droplet shape can be neglected and the droplet shape can be reasonably assumed as a spherical
154 cap. Before droplet deposition, both CCD and IR thermography acquisitions are started, and the
155 evolution of droplet profile is recorded in time. Since the dosing system is also located inside the
156 environmental chamber, the temperature of both liquid desiccant and water before deposition can be
157 considered to be in equilibrium with that of the ambient.

158 Table 1 Properties of 54% wt. LiBr solution and distilled water as specific heat capacity c_p (kJ/kg/K);
159 density ρ (kg/m^3); liquid-gas surface tension γ_{lg} (mN/m); dynamic viscosity υ (mPa·s); thermal
160 conductivity k (W/m/K); and saturation temperature T_{sat} (°C). Properties shown were obtained at
161 20 °C and at 1 atm.

Liquid type	c_p (kJ/kg/K)	ρ (kg/m^3)	γ_{lg} (mN/m)	υ (mPa·s)	k (W/m/K)	T_{sat} (°C)
54% wt. LiBr solution	1.98	1600	91.54	4.751	0.429	140
Distilled water	4.18	998	72.75	1.005	0.598	100

162 Table 2 Properties of PTFE substrate as density ρ (kg/m^3); specific heat capacity c_p (kJ/kg/K); thermal

conductivity k (W/m/K); thermal diffusivity α (m^2/s), $\alpha = k/\rho c_p$; substrate thickness δ (mm); surface roughness S_q (μm); and equilibrium contact angle for a 3 μL water droplet, $\theta_{0,W}$ (°), and LiBr-H_2O droplet, $\theta_{0,S}$ (°), at 20 °C and 1 atm.

Material	ρ (kg/m^3)	c_p (kJ/kg/K)	k (W/m/K)	α (m^2/s)	δ (mm)	S_q (μm)	Equilibrium $\theta_{0,W}$ (°)	Equilibrium $\theta_{0,S}$ (°)
PTFE	2200	1.05	0.25	0.52	10.0	0.357	95° ± 3°	101 ± 3°

3. EXPERIMENTAL RESULTS

3.1. Evolution of droplet profile

Figure 3 shows typical profile evolution of LiBr-H_2O droplets at 45°C and humidity of 30%*RH*, 60%*RH*, 90%*RH*. Figure 4 represents the variation of the contact angle, θ (deg), and the non-dimensional contact radius, R/R_0, of LiBr-H_2O droplets versus non-dimensional time (normalized by the experimental duration), τ. On a smooth PTFE substrate, the initial contact angle of LiBr-H_2O droplet is *ca.* 101°± 3°. As vapor absorbs into the droplet, an expansion in volume is recorded especially when the ambient humidity is high. The droplet expansion is demonstrated by the simultaneous increase in droplet height and contact radius, while the droplet contact angle remains almost constant throughout the entire experimental duration. At high humidity conditions of 90% *RH*, the contact angle decreases by *ca.* 5°, which is attributed to the decreasing liquid-air surface tension as the desiccant solution gets diluted due to water uptake. On the other hand, the contact radius increases depending on the ambient humidity. When the ambient humidity is low, *e.g.* 30% *RH*, the contact radius increases slightly to about 1.03~1.05 times of its initial value after 10 minutes. At ambient humidity of 60% *RH*, the contact radius increases more significantly to 1.14~1.20 times of its initial value after 30 minutes. At higher ambient humidity of 90% *RH*, the contact radius of LiBr-H_2O droplet keeps increasing to about 1.6 times of its initial value.

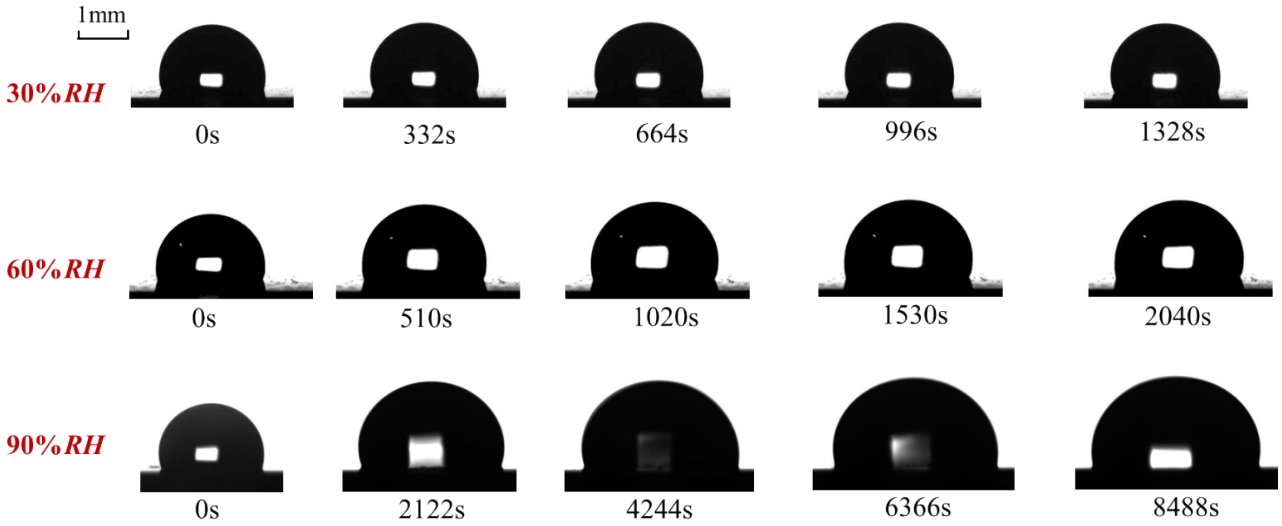

Figure 3 Profile evolution of LiBr-H_2O droplets during vapor absorption for ambient condition of 45℃ and 30% *RH*, 60% *RH*, 90% *RH*, for $\tau = 0$, $\tau = 0.25$, $\tau = 0.5$, $\tau = 0.75$ and $\tau = 1$.

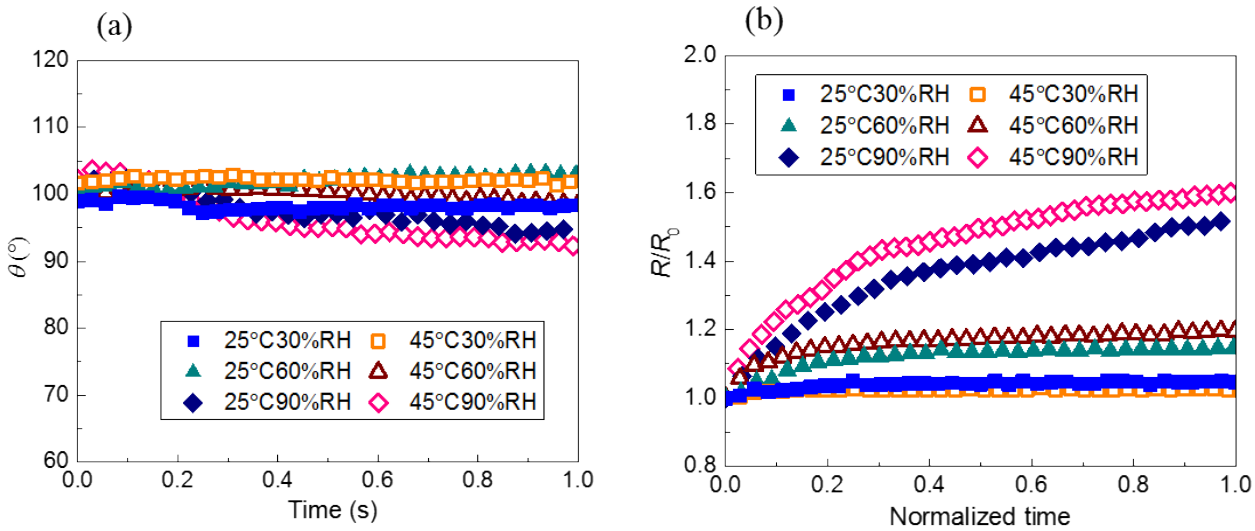

Figure 4 Evolution of (a) contact angle θ (deg), and (b) non-dimensional contact radius R/R_0, of LiBr-H_2O droplets, versus non-dimensional time, τ, for (closed symbols) T_{amb} = 25 ℃ and (open symbols) T_{amb} = 45 ℃ at (square) 30% *RH*, (up-triangles) 60% *RH*, and (diamonds) 90% *RH* on smooth PTFE.

For direct comparison, Figure 5 and Figure 6 include the behavior of pure water droplets during evaporation on the same substrate for the same six experimental conditions. The initial contact angle of pure water droplet is 95°±5°, lower than that of LiBr-H_2O droplet, which is attributed to the lower liquid-air surface tension, 72.75 mN/m, compared to 54 wt.% LiBr-H_2O solution (91.54 mN/m). Pure water droplets firstly evaporate following the constant contact radius (CCR) mode, where R/R_0 remains

almost constant and θ decreases along with time to account for the loss of volume for the first 20% of the droplet lifetime. Thereafter, as the contact angle decreases to approximately 86°±3°, the contact line starts receding and droplets evaporate in the constant contact angle (CCA) mode, where θ remains almost constant, and R/R_0 monotonically decreases. The CCA mode lasts for approximately 60% of the overall droplet lifetime. Lastly, as the droplet becomes smaller, towards the end of the evaporation process, droplet evaporation turns into a mixed mode where both θ and R/R_0 decrease, which takes approximately the remaining 20% droplet lifetime. The three distinctive regimes reported here, *i.e.*, CCR, then CCA and lastly the mixed mode, are in agreement with previous studies [11,33-35] on water droplets evaporating on smooth PTFE substrates.

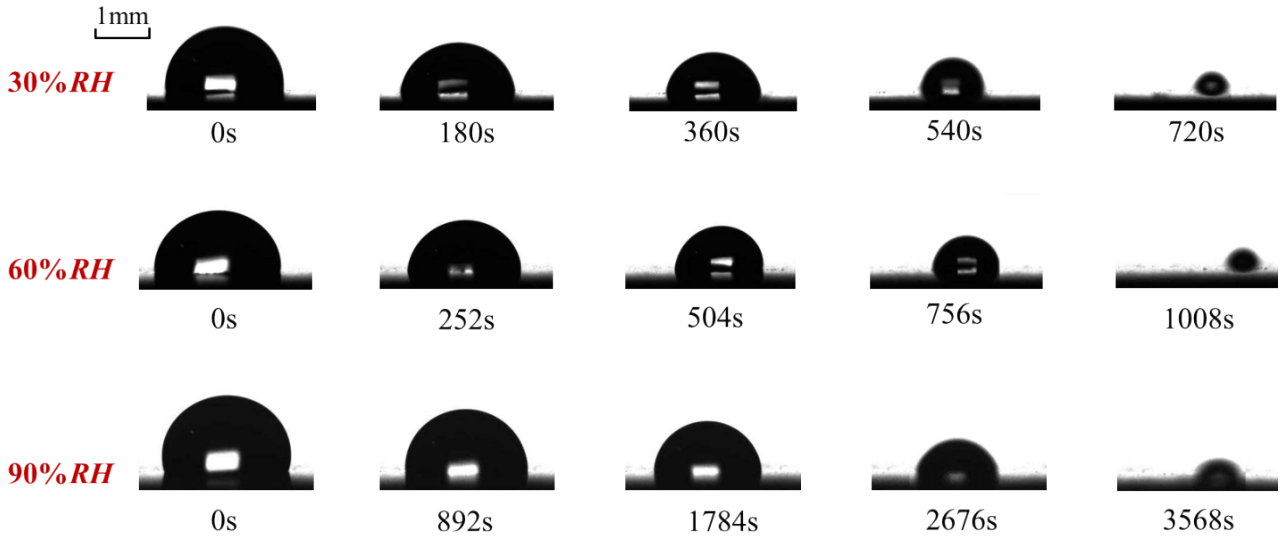

Figure 5 Profile evolution of pure water droplets during evaporation for ambient condition of 45℃ and 30% *RH*, 60% *RH*, 90% *RH*, for $\tau = 0$, $\tau = 0.25$, $\tau = 0.5$, $\tau = 0.75$ and $\tau = 1$.

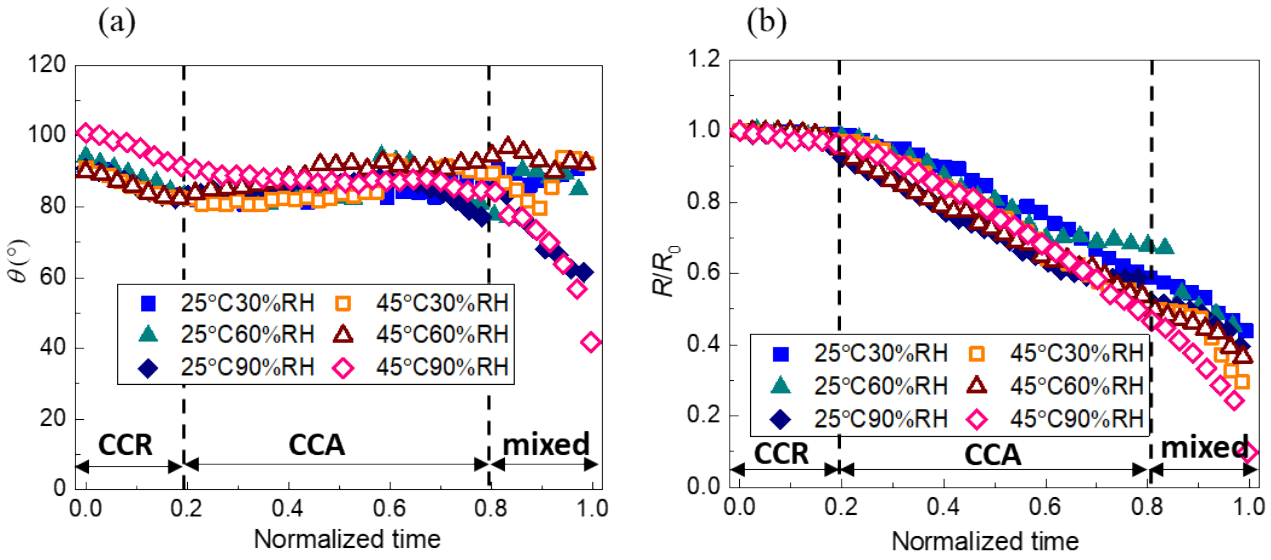

Figure 6 Evolution of (a) contact angle θ (deg), and (b) non-dimensional contact radius R/R_0 of pure water droplets, versus non-dimensional time, τ, for (closed symbols) T_{amb} = 25 °C and (open symbols) T_{amb} = 45 °C at (square) 30% *RH*, (up-triangles) 60% *RH*, and (diamonds) 90% *RH* on smooth PTFE.

3.2. Evolution of droplet volume

Figure 7 presents the volume evolution of LiBr-H_2O droplets during vapor absorption and that of pure water droplets during evaporation. Moreover, initial vapor absorption and evaporation rates for the six experimental conditions are included in Table 3.

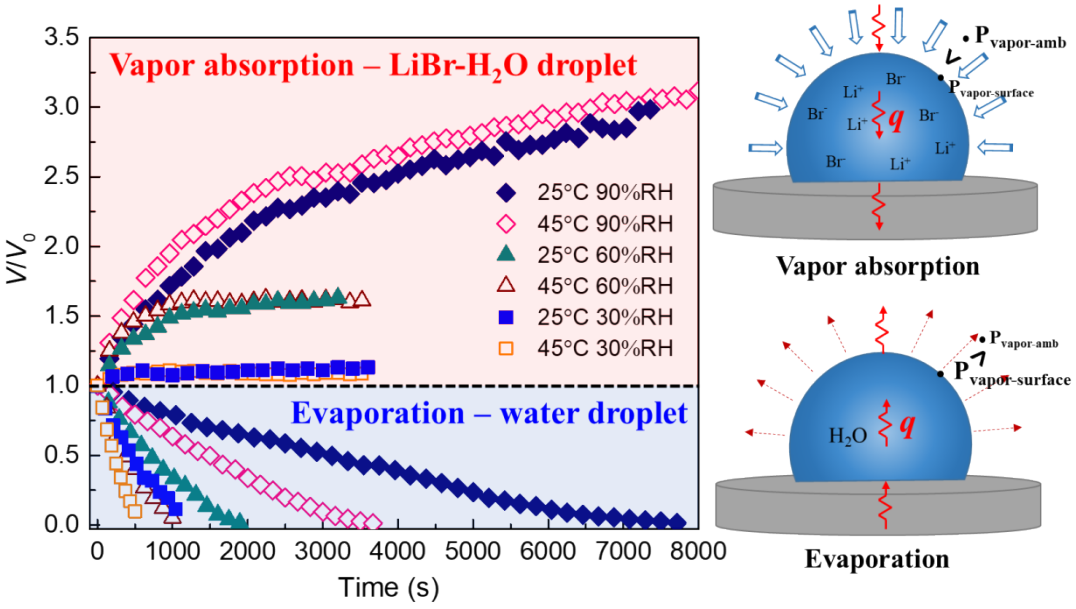

Figure 7 Evolution of non-dimensional droplet volume with respect to the original volume, V/V_0, along with time, t (s), during vapor absorption and evaporation for the six environmental conditions.

Table 3 Initial evaporation rate, -dV/dt, and initial vapor absorption rate, dV/dt, for the six experimental conditions. (We note here that at 30% *RH*, the vapor absorption is very small, thus calculations are only carried out for 60% *RH* and 90% *RH* conditions)

Condition	25°C30%*RH*	25°C60%*RH*	25°C90%*RH*	45°C30%*RH*	45°C60%*RH*	45°C90%*RH*
Absorption rate *dV/dt* (nL/s)	-	4.20	4.59	-	5.96	6.97
Evaporation rate -*dV/dt* (nL/s)	4.25	3.02	0.83	9.42	5.40	1.27

From both Figure 7 and Table 3, it is clear that both evaporation and vapor absorption rates are strongly function of the ambient condition. In the case of LiBr-H_2O droplets, both ambient temperature and relative humidity have an impact on the initial instantaneous vapor absorption rate, whereas the final droplet volume is only function of the relative humidity. From Table 3 the vapor absorption rate increases with ambient temperature and with relative humidity. For the presented cases, the initial vapor absorption rate follows the order of $dV/dt|_{45°C90\%RH} > dV/dt|_{45°C60\%RH} > dV/dt|_{25°C90\%RH} > dV/dt|_{25°C60\%RH}$. Regardless of ambient temperature, the final normalized volume is almost the same for the same relative humidity: V/V_0 (30% *RH*) ≈ 1.1, V/V_0 (60% *RH*) ≈ 1.6 and V/V_0 (90% *RH*) ≈ 3.0 ~ 3.5. In the case of pure water droplets, the evaporation rate increases with ambient temperature, while it decreases with increasing relative humidity. For the six experimental conditions, the evaporation rate follows an order of $-dV/dt|_{45°C30\%RH} > -dV/dt|_{45°C60\%RH} > -dV/dt|_{25°C30\%RH} > -dV/dt|_{25°C60\%RH} > -dV/dt|_{45°C90\%RH} > -dV/dt|_{25°C90\%RH}$ as presented in Table 3.

4. ANALYSIS AND DISCUSSION

4.1. Heat transfer analysis

Within the droplet, both heat convection and heat conduction may occur, which can be evaluated

by the Péclet number expressed as Eq. (1).

$$Pe=\rho c_p UR/k, \quad (1)$$

where R is the droplet contact radius, ρ is the density, c_p is the heat capacity, U is the radial flow velocity within the droplet, and k is the thermal conductivity of the liquid studied. For evaporation of water droplets with contact angles *ca.* 90°, the evaporative mass flux can be regarded as uniform across the droplet interface [11, 36, 37]. In this case, the radial flow velocity, U, is rather low in the order of 10^{-7} m/s. In the case of liquid-desiccant droplets where the water vapor diffuses towards the droplet interface, homogeneous absorption flux is also expected for contact angles *ca*. 90°. Hence, the concentration gradient along the droplet surface is rather small, and the concentration-induced Marangoni effect can therefore be neglected. Moreover, the IR images measured at the liquid-gas interface also show the homogeneity of the temperature profile and the absence of thermal gradients (Fig. 8(a) & Fig. 8(b)). In view of the above, we can then safely state that the radial flow velocity, U, remains small and is not further enhanced by the presence of Marangoni flows. Then, the *Pe* number is estimated as << 1 [38], confirming that the convective heat transfer within the droplet is negligible [39-41].

The heat conduction process within the droplet can be further evaluated by the characteristic time, τ^*, given by Eq. (2).

$$\tau^* = \rho c_p h^2/k, \quad (2)$$

where h is the droplet height. Taking into account the thermal properties of the LiBr-H_2O droplets and water droplets reported in Table 1, τ^*_{LiBr} is calculated as 10.51 s, and τ^*_{Water} is *ca.* 9.91s. Right after the deposition of a liquid desiccant droplet, a temperature profile within the droplet may develop during the first instants of the vapor absorption process. However, compared to the overall droplet lifetime

255 (~10^3 seconds), the characteristic time for heat conduction is quite short, ~1% of the total lifetime. The
256 timescale analysis indicates that the heat flux induced by evaporation or absorption can timely diffuse
257 throughout the droplet volume so as to even out the temperature gradient within the droplet bulk, and
258 we can consider the temperature distribution within the droplet as homogenous ($\nabla^2 T_{drop} = 0$) during
259 most of the droplet lifetime.

260 Even though the spatial temperature distribution across the droplet is homogenous, the average
261 surface temperature of LiBr-H_2O droplets varies slowly along with time as a result of the balance
262 between heat absorption and dissipation. To provide further evidences on the temperature evolution,
263 Figure 8 shows the average temperature at the droplet surface in time along with characteristic IR
264 thermography snapshots. It shows that the temperature distribution along the droplet surface is nearly
265 uniform throughout the vapor absorption process, which demonstrates experimentally the above
266 timescale analysis of heat transfer within the droplet. The droplet surface experiences the highest
267 temperature right after being deposited on the substrate. This indicates that vapor absorption starts as
268 the droplet is generated from the needle and gets in contact with humid air. The released heat due to
269 vapor-to-water phase change and absorption causes the observed temperature increase when respect to
270 ambient conditions. After being deposited on the substrate, the absorbed heat is at the same time
271 dissipated both through heat conduction towards the substrate, and through convective heat transfer
272 into the ambient air. As a combined result of heat dissipation and decreasing absorption rate, the droplet
273 surface gradually cools down towards equilibrium with the ambient as indicated by Figure 8. In the
274 case of pure water, droplets experience the lowest surface temperature right after being deposited as
275 they cool down due to evaporative cooling, then gradually warm up as they reach equilibrium with the

ambient.

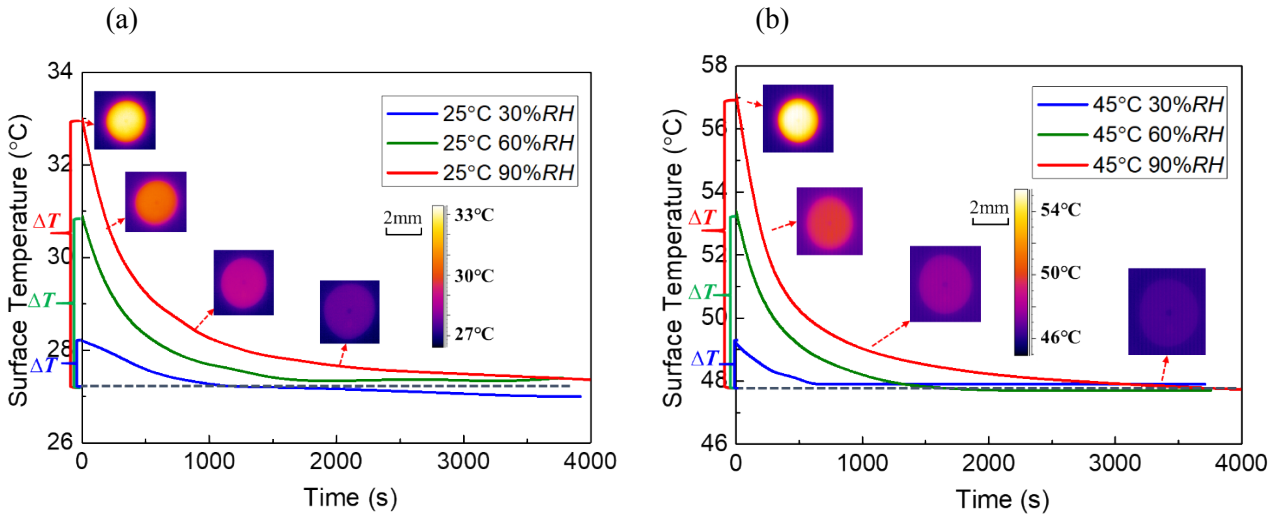

Figure 8 Evolution of average temperature at droplet surface and corresponding IR images during vapor absorption for ambient conditions of 30% *RH*, 60% *RH*, 90% *RH*, and (a) 25 °C, (b) 45 °C.

Figure 9 summarizes the surface temperature increase of LiBr-H_2O droplets and decrease of pure water droplets right after droplet deposition for the six experimental conditions. The initial temperature change depends strongly on the ambient temperature and relative humidity. In general, the initial temperature variation is more noticeable at high ambient temperature (45 °C) than at low temperature (25 °C) independently of the liquid or the relative humidity studied. For the same ambient temperature, the initial temperature rise of LiBr-H_2O droplets is more apparent at high relative humidity conditions, while the initial temperature decrease for pure water droplets becomes smaller at high relative humidity conditions. Typically, the increase in the surface temperature of a liquid desiccant droplet is function of the absorption rate, while the decrease in the surface temperature of a water droplet is proportional to the evaporation rate. Then, quantitative calculations of the average heat flux into the droplet surface can be carried out based on the surface area and on the vapor absorption rate, or the evaporation rate in the case of water droplets, by making use of eq. (3). Vapor absorption and evaporation rates are

calculated for the first instants right after droplet deposition.

$$\Phi_q = \frac{\dot{Q}}{S} = \frac{L_{vl}\rho\frac{dV}{dt}}{\pi\left(h^2+R^2\right)}, \tag{3}$$

Where Φ_q represents the average heat flux across the droplet surface, kW/m^2, $\dot{Q}$ is the rate of heat flow, kW, S repsrents the area of droplet surface, m^2, and L_{vl} is the latent heat released during vapor-liquid phase change, kJ/kg. The calculation results are summarized in Table 4.

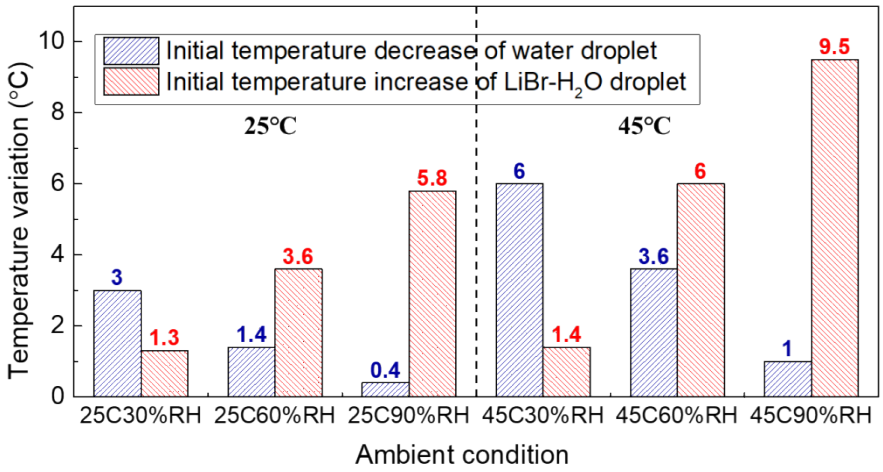

Figure 9 Initial temperature increase of LiBr-H_2O droplet caused by absorption heating (red columns), and temperature decrease of pure water droplet caused by evaporation cooling (blue columns) for the six experimental conditions.

Table 4 Average heat flux, Φ_q (kW/m^2), at the interface of LiBr-H_2O droplets and pure water droplets induced by absorption heating and evaporation cooling, respectively. (Calculation results based on the vapor absorption rate and evaporation rate right after droplet deposition.)

Φ_q (kW/m^2)	25°C30%*RH*	25°C60%*RH*	25°C90%*RH*	45°C30%*RH*	45°C60%*RH*	45°C90%*RH*
LiBr-H_2O droplet	0.507	1.066	1.166	0.472	1.512	1.771
Pure water droplet	1.132	0.812	0.216	2.848	1.443	0.333

The heat flux induced by absorption heating or evaporative cooling differs depending on the ambient condition. In the case of LiBr-H_2O droplets, the absorption heat flux follows the order of $\Phi_{q,45°C90\%RH} > \Phi_{q,45°C60\%RH} > \Phi_{q,25°C90\%RH} > \Phi_{q,25°C60\%RH} > \Phi_{q,25°C30\%RH} \approx \Phi_{q,4530\%RH}$, which corresponds

with the order of initial temperature rise in the six experimental conditions. Since vapor absorption is driven by the partial pressure difference between the ambient and the droplet surface, at low relative humidity conditions, *i.e.*, small gradient of concentration, the vapor absorption rate is rather low, hence similar values of average heat flux are reported for 30% *RH* conditions in Table 4. In the case of pure water droplets, the heat flux caused by evaporative cooling follows the order of $\Phi_{q,45°C30\%RH}$ > $\Phi_{q,45°C60\%RH}$ > $\Phi_{q,25°C30\%RH}$ > $\Phi_{q,25°C60\%RH}$ > $\Phi_{q,45°C90\%RH}$ > $\Phi_{q,25°C90\%RH}$, which also corresponds with the order of initial temperature decrease at the surface of water droplets. For water droplets, evaporation is driven by the partial pressure difference from the droplet surface to the ambient; hence the high relative humidity conditions hinder droplet evaporation and the evaporative cooling effect. The quantitative calculations included above stress that the heat flux induced by absorption heating and evaporative cooling is the dominating factor for the initial temperature variation at the droplet surface during and right after droplet deposition. To accurately estimate the water vapor pressure at the droplet surface, the following mass transfer analysis takes into account the concentration variation within the droplet bulk and the temperature variation at the droplet surface captured by IR thermograph.

4.2. Mass transfer analysis

The mass transfer process includes the vapor diffusion on the air side, the vapor-water transition at the droplet interface, and the solute diffusion on the droplet side. Typically, the mass diffusion rate in the gas phase is 10^3~10^4 times of that in the liquid phase ($D_{\mathrm{water/air}}/D_{\mathrm{LiBr/LiBr-H_2O}} \sim 10^{-5}/10^{-9} \sim 10^4$) [42]. Therefore, the vapor absorption rate is limited by the mass diffusion process on the liquid side [31]. The solute diffusion rate, D_l, on the liquid phase is related to the liquid temperature, T, and dynamic viscosity, μ, according to the Stokes-Einstein equation [43]. For the cases of 45 °C and 25 °C,

the ratio of solute diffusion rate within the droplet can be calculated as Eq. (4).

$$D_{\mathrm{l}} = \frac{k_B T}{6\pi\mu r},\ \frac{D_{T_1}}{D_{T_2}} = \frac{T_1}{T_2}\frac{\mu_{T_2}}{\mu_{T_1}},\ \frac{D_{\mathrm{l},45^\circ\mathrm{C}}}{D_{\mathrm{l},25^\circ\mathrm{C}}} = \frac{318.15}{298.15}\frac{0.004286}{0.002963} \approx 1.54, \tag{4}$$

where k_B represents the Boltzmann's constant, and r is the radius of the spherical particle, *i.e.*, the Li^+ and Br^- ions.

The above calculation presented in Eq. (4) shows that the solute diffusion rate at 45 °C is 50% greater than that at 25 °C. Hence, at higher temperature, the solute diffuses more effectively from the high concentration at the droplet bulk towards the interface. Then, droplets at higher temperature can maintain a relatively higher solute concentration at the droplet interface. In response to the higher salt concentration at the droplet interface, the vapor pressure is lower, and therefore the vapor absorption rate at 45 °C is higher when compared to 25 °C especially at the initial stage of vapor absorption. The greater absorption rates at high temperatures presented (in Table 3) in turn induce greater average heat flux and a further increase of the surface temperature (see Table 4 and Figure 9, respectively).

The vapor pressure at the droplet interface, $P_{\mathrm{vapor,surface}}$, can be evaluated according to the fitting correlations derived by Patek and Klomfar (Eqs. (5) and (6)) [44].

$$P_{vapor,surface} = P_{sat}\left(\Theta\right) \tag{5}$$

where P_{sat} is the saturation vapor pressure of pure water at "shifted temperature", Θ, due to the presence of dissolved salts. Θ is function of the mole fraction, x_{mole}, and temperature, T, of LiBr-H_2O solution, and can be calculated as Eq. (6).

$$\Theta = T - \sum_{i=1}^{8} a_i \left(x_{mole}\right)^{m_i} \left|0.4 - x_{mole}\right|^{n_i} \left(\frac{T}{T_c}\right)^{t_i} \tag{6}$$

where T_{c} is the critical temperature of pure water, 647.096 K, a = {-2.41303×10^2, 1.91750×10^7, -

343 1.75521×10^{8}, 3.25432×10^{7}, 3.92571×10^{2}, -2.12626×10^{3}, 1.85127×10^{8}, 1.91216×10^{3}}, m = {3, 4, 4, 8,
344 1, 1, 4, 6}, n = {0, 5, 6, 3, 0, 2, 6, 0}, t = {0, 0, 0, 0, 1, 1, 1, 1}, and the mole fraction, x_{mole}, is calculated
345 by Eq. (7).

$$x_{mole} = \frac{x/M_{\text{LiBr}}}{x/M_{\text{LiBr}} + (1-x)/M_{\text{H}_2\text{O}}}, \tag{7}$$

346 where x is the mass fraction of LiBr solute in LiBr-H_2O solution, and M represents the molar mass.
347 Since the initial concentration of the LiBr-H_2O solution is known, any increase in the droplet volume
348 is due to water absorbed, from experimental observations of droplet profile evolution in time, the mass
349 fraction of LiBr can be estimated.

350 Then, combining Eq. (5), (6) and (7), the vapor pressure difference can be calculated. Because the
351 vapor absorption rate is low and no apparent volume increase is observed at low relative humidity of
352 30% *RH*, in the following calculations we only consider 60% and 90% relative humidity conditions.
353 Figure 10(a) shows the evolution of vapor pressure difference between the droplet interface and the
354 ambient air during vapor absorption. From experimental observations of droplet profile, the vapor
355 absorption rate is estimated in time, which is presented in Figure 10(b). Both Figure 10(a) and 10(b)
356 clearly indicate that vapor pressure differences and absorption rates are greater right after droplet
357 deposition, independently of the condition studied. As vapor absorption proceeds and the droplet gets
358 diluted, the vapor pressure difference between the ambient and the droplet surface diminishes and so
359 does the vapor absorption rate. Moreover, the order of initial vapor pressure difference, $\Delta P|_{45°C90\%RH} >$
360 $\Delta P|_{45°C60\%RH} > \Delta P|_{25°C90\%RH} > \Delta P|_{25°C60\%RH}$, corresponds with the order of initial vapor absorption rate
361 for the four experimental conditions, $dV/dt|_{45°C90\%RH} > dV/dt|_{45°C60\%RH} > dV/dt|_{25°C90\%RH} >$
362 $dV/dt|_{25°C60\%RH}$.

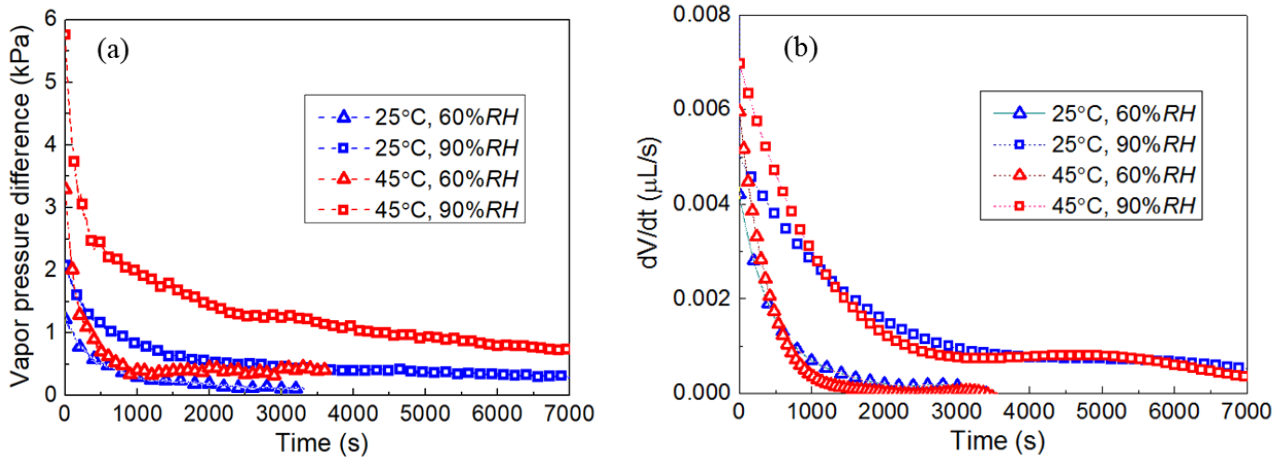

Figure 10 Evolution of (a) calculated vapor pressure difference, ΔP (kPa), between the droplet interface and ambient air, and (b) rate of droplet volume increase, dV/dt (μL/s) during vapor absorption on PTFE substrates for ambient conditions of 25 °C, 45 °C, and 60% *RH*, 90% *RH*.

According to Eqs. (5) and (6), the influence of $T_{surface}$ and x_{LiBr} on the vapor pressure at the droplet surface, $P_{vapor,surface}$, are opposite. On one hand, the increase in $T_{surface}$ induces the increase of $P_{vapor,surface}$, while on the other hand, the increase in x_{LiBr} causes the decrease of $P_{vapor,surface}$. Therefore, for constant ambient conditions, *i.e.*, constant P_{amb}, the driving force for vapor absorption, $\Delta P = P_{amb} - P_{vapor,surface}$, depends strongly on both $T_{surface}$ and x_{LiBr}. As the vapor absorption process proceeds, both $T_{surface}$ and x_{LiBr} decrease with time. The decreasing $T_{surface}$ tends to increase ΔP, whereas the decreasing x_{LiBr} tends to decrease ΔP. Results on the evolution of the vapor absorption driving force ΔP included in Figure 10(a) show a clear decreasing trend of ΔP along with vapor absorption time. The decreasing ΔP indicates that the influence of x_{LiBr} on ΔP greatly outweighs the influence of $T_{surface}$. As the droplet gets further diluted, the driving force decreases along with time due to the decrease in x_{LiBr}, and the vapor absorption rate decreases accordingly as demonstrated in Figure 10(b).

4.3. Comparison with droplet evaporation

Based on the experimental results and analyses presented above, the main features during droplet

379 evaporation and vapor absorption are summarized in Table 5.

380 Table 5 Summary of features during droplet evaporation and vapor absorption on smooth hydrophobic PTFE
381 substrates (TCL: triple contact line, *RH*: relative humidity, CCR: constant contact radius).

Comparison	Vapor absorption	Water evaporation
Droplet profile	Expands with advancing TCL	Shrinks with receding TCL
Rate of evaporation/ vapor absorption	Increases with temperature and increases with *RH*	Increases with temperature and decreases with *RH*
Heat transfer	Absorptive heating effect $T_{surface}$ increases initially, then decreases along with time	Evaporative cooling effect $T_{surface}$ decreases initially, then increases along with time
Mass transfer	Solute diffusion dominates	Vapor diffusion dominates
Driving force	Decreases along with time Volume increases in a saturation trend	Constant if neglecting evaporative cooling Volume decreases linearly for droplets in the CCR mode

382 In the psychrometric chart in Figure 11, solid black lines present the iso-relative humidity curves
383 of humid air at 20% *RH*, 40% *RH*, 60% *RH*, 80% *RH*, 100% *RH*, while the dashed black lines present
384 the iso-concentration curves of LiBr-H_2O solution at 20 wt.%, 30 wt.%, 40 wt.%, 50 wt.%, 60 wt.%.
385 For pure water droplets, the droplet liquid-air interface is always saturated. During evaporation, the
386 physical state of the droplet liquid-air interface as humidity ratio (y-axis) versus temperature (x-axis)
387 transits from W_0 to W_1 along the saturation line (100% *RH* or 0 wt. % solute concentration), as marked
388 with blue arrows in Figure 11. After droplet deposition, the droplet experiences a decrease in interfacial
389 temperature due to evaporative cooling, and as the droplet attains equilibrium with the ambient, the
390 interfacial temperature increases. For the high humidity case 90% *RH* (Figure 11 (a)), the temperature
391 at the droplet surface increases from 45 °C to T_{amb}, *ca.* 46 °C, while for the low humidity case 30%
392 *RH* (Figure 11 (b)) the temperature increases from 40 °C to T_{amb}, *ca.* 45 °C. It is noteworthy to mention
393 that at low ambient humidity conditions such as 30% *RH*, the effect of evaporative cooling is stronger

394 due to the greater driving force, ΔP, hence the initial surface temperature is lower, and the variation of
395 droplet interfacial temperature is more apparent as presented in Figure 11(a).

396 On the psychrometric chart, the state point of LiBr-H_2O droplet indicates the solute concentration
397 (dotted curve) within the droplet bulk, as well as the relative humidity (solid curve), temperature (*x*-
398 axis), and humidity ratio (*y*-axis) of the equilibrium humid air layer near the droplet interface. In Figure
399 11, the state variations of LiBr-H_2O droplets during vapor absorption are marked with red arrows from
400 S_0 to S_1. Different from pure water droplets, the vapor pressure at the surface of LiBr-H_2O droplets is
401 much lower. For 54 wt.% LiBr-H_2O droplets, the vapor pressure is theoretically in equilibrium with
402 low humidity air of *ca.* 20% *RH*. As vapor absorption proceeds, LiBr-H_2O droplets get diluted with
403 decreasing salt concentration due to water uptake. As a result, the state of LiBr-H_2O droplet moves
404 across the iso-concentration curves shown in the psychrometric chart and toward equilibrium with the
405 humid atmosphere. Moreover, the heat released due to vapor-water phase change also causes the
406 temperature increase in the droplet surface at early stages shown as the initial state points of LiBr-H_2O
407 droplets in Figure 11. At high ambient humidity such as 90% *RH*, the salt concentration of LiBr-H_2O
408 droplet decreases more markedly due to the large amount of water uptake, which induces a stronger
409 absorptive heating effect. Therefore, in high humidity cases, the state point moves across the iso-
410 concentration curves with greater temperature decrease as marked with red arrow, $S_0 \rightarrow S_1$, in Figure
411 11(b).

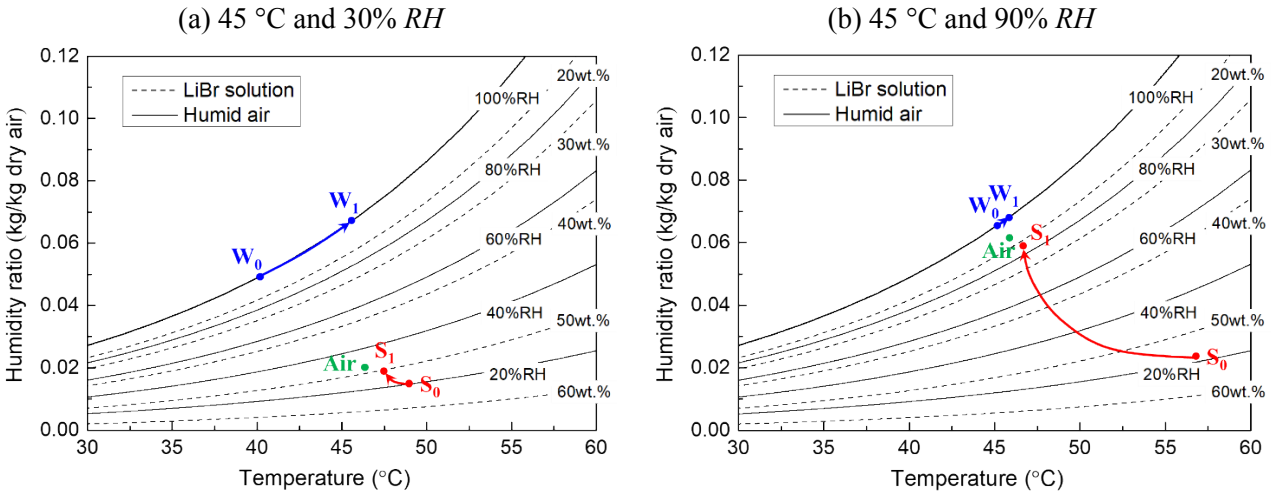

Figure 11 Psychrometric chart of humid air at different relative humidity (solid lines), and equivalent humid air layer at the surface of LiBr-H_2O solution with different concentrations (dashed lines). Marks inside the graph presents the state of ambient air bulk (Green points, Air), the state variations of droplet during evaporation (blue arrows, $W_0 \rightarrow W_1$) and during vapor absorption (red arrows, $S_0 \rightarrow S_1$) for ambient conditions of 45 °C, and (a) 30% *RH*, (b) 90% *RH*.

5. CONCLUSION

The coupled heat and mass transfer process during vapor absorption into LiBr-H_2O droplet has been experimentally investigated under controlled environmental conditions. Due to the strong adhesion force of LiBr salt ions to water molecules, the vapor pressure at the droplet surface is greatly reduced, and water vapor diffuses from the air side to the liquid side, causing the growth of the droplet volume. Along with water vapor absorption, heat of absorption is released inducing a temperature increase at the droplet surface. IR thermography shows that desiccant droplets experience the highest surface temperature right after being deposited on the substrate, and then gradually cool down as a combined result of the decreasing vapor absorption rate and the heat dissipation into the substrate and into the ambient. Moreover, the initial temperature rise at the droplet surface is quantitatively in agreement with the absorption heat flux depending on the ambient conditions studied.

The variation of surface temperature, in turn influences the vapor pressure at the droplet surface

429 and hence the vapor diffusion on the air side. The vapor pressure difference between the ambient air
430 and the droplet surface is evaluated taking into account the evolution of the surface temperature as well
431 as the evolution of the salt concentration in the droplet bulk. Along with water uptake, the desiccant
432 solution gets gradually diluted, and the vapor pressure difference between the ambient air and the
433 droplet surface decreases along with time. We conclude on the need to couple the heat and mass
434 transfer mechanisms taking place during vapor absorption into liquid desiccant droplets for accurately
435 predicting this phenomenon. Furthermore, similarities and differences in the mechanisms governing
436 vapor absorption into liquid desiccant droplets and those of water droplet evaporation have been
437 summarized.

438 ## Acknowledgements

439 The authors gratefully acknowledge the support received by the International Institute for Carbon-
440 Neutral Energy Research (WPI-I^{2}CNER). ZW acknowledges the support received by the Japanese
441 Society for the Promotion of Science (JSPS). DO gratefully acknowledges the support received from
442 JSPS KAKENHI (Grant no. JP16K18029 and JP18K13703). KS acknowledges the support received
443 from EPSRC through the grant number EP/N011341/1. All the authors thank Dr. Prashant Valluri for
444 sharing his ideas and providing valuable suggestions on the theoretical analysis.

445 ## References

446 [1] Chua, K. J., Chou, S. K., & Yang, W. M. "Liquid desiccant materials and dehumidifiers – A
447 review." *Renewable & Sustainable Energy Reviews* 56 (2016):179-195.

448 [2] Mei, L., & Dai, Y. J. "A technical review on use of liquid-desiccant dehumidification for air-conditioning
449 application." *Renewable & Sustainable Energy Reviews* 12.3 (2008):662-689.

450 [3] Chua, K. J., Chou, S. K., & Yang, W. M. "Advances in heat pump systems: A review." *Applied*

Energy 87.12 (2010): 3611-3624.

[4] Parham, K., Khamooshi, M., Tematio, D. B. K., Yari, M., & Atikol, U. "Absorption heat transformers–a comprehensive review." *Renewable and Sustainable Energy Reviews* 34 (2014): 430-452.

[5] Wang, Z., Zhang, X., & Li, Z. "Evaluation of a flue gas driven open absorption system for heat and water recovery from fossil fuel boilers." *Energy Conversion and Management* 128 (2016): 57-65.

[6] Liu, X. H., Zhang, Y., Qu, K. Y., & Jiang, Y. "Experimental study on mass transfer performances of cross flow dehumidifier using liquid desiccant." *Energy Conversion and Management* 47.15 (2006): 2682-2692.

[7] Longo, G. A., & Gasparella, A. "Experimental and theoretical analysis of heat and mass transfer in a packed column dehumidifier/regenerator with liquid desiccant." *International Journal of Heat and Mass Transfer* 48.25 (2005): 5240-5254.

[8] Dai, Y. J., & Zhang, H. F. "Numerical simulation and theoretical analysis of heat and mass transfer in a cross flow liquid desiccant air dehumidifier packed with honeycomb paper." *Energy Conversion and Management* 45.9 (2004): 1343-1356.

[9] Wang, Z., Zhang, X., & Li, Z. "Investigation on the coupled heat and mass transfer process between extremely high humidity air and liquid desiccant in the counter-flow adiabatic packed tower." *International Journal of Heat and Mass Transfer* 110 (2017): 898-907.

[10] Hu, H., & Larson, R. G. "Evaporation of a sessile droplet on a substrate." *The Journal of Physical Chemistry B* 106.6 (2002): 1334-1344.

[11] Dash, S., & Garimella, S. V. "Droplet evaporation dynamics on a superhydrophobic surface with negligible hysteresis." *Langmuir* 29.34 (2013): 10785-10795.

[12] Sefiane, K., Wilson, S. K., David, S., Dunn, G. J., & Duffy, B. R. "On the effect of the atmosphere on the evaporation of sessile droplets of water." *Physics of Fluids* 21.6 (2009): 062101.

[13] Fukatani, Y., Orejon, D., Kita, Y., Takata, Y., Kim, J., & Sefiane, K. "Effect of ambient temperature and relative humidity on interfacial temperature during early stages of drop evaporation." *Physical Review E* 93.4 (2016): 043103.

[14] Stauber, J. M., Wilson, S. K., Duffy, B. R., & Sefiane, K. "On the lifetimes of evaporating droplets." *Journal of Fluid Mechanics* 744 (2014): R2 1-12.

[15] Rose, J. W. "Dropwise condensation theory and experiment: a review." *Proceedings of the Institution of Mechanical Engineers, Part A: Journal of Power and Energy* 216.2 (2002): 115-128.

[16] Boreyko, J. B., & Chen, C. H. "Self-propelled dropwise condensate on superhydrophobic surfaces." *Physical Review Letters* 103.18 (2009): 184501.

[17] Enright, R., Miljkovic, N., Alvarado, J. L., Kim, K., & Rose, J. W. "Dropwise condensation on micro-and nanostructured surfaces." *Nanoscale and Microscale Thermophysical Engineering* 18.3 (2014): 223-250.

[18] Soulié, V., Karpitschka, S., Lequien, F., Prené, P., Zemb, T., Moehwald, H., & Riegler, H. "The evaporation behavior of sessile droplets from aqueous saline solutions." *Physical Chemistry Chemical*

Physics 17.34 (2015): 22296-22303.

[19] Brenn, G. "Concentration fields in evaporating droplets." *International Journal of Heat and Mass Transfer* 48.2 (2005): 395-402.

[20] Misyura, S. Y. "High temperature nonisothermal desorption in a water–salt droplet." *International Journal of Thermal Sciences* 92 (2015): 34-43.

[21] Misyura, S. Y. "Evaporation and heat and mass transfer of a sessile drop of aqueous salt solution on heated wall." *International Journal of Heat and Mass Transfer* 116 (2018): 667-674.

[22] Misyura, S. Y. "Evaporation and heat transfer of aqueous salt solutions during crystallization." *Applied Thermal Engineering* 139 (2018): 203-212.

[23] Zhong, X., Ren, J., & Duan, F. "Wettability effect on evaporation dynamics and crystalline patterns of sessile saline droplets." *The Journal of Physical Chemistry B* 121.33 (2017): 7924-7933.

[24] McBride, S. A., Dash, S., & Varanasi, K. K. "Evaporative Crystallization in Drops on Superhydrophobic and Liquid-Impregnated Surfaces." *Langmuir* 34. 41 (2018): 12350-12358.

[25] Shahidzadeh-Bonn, N., Rafaı, S., Bonn, D., & Wegdam, G. "Salt crystallization during evaporation: impact of interfacial properties." *Langmuir* 24.16 (2008): 8599-8605.

[26] Kaya, D., Belyi, V. A., & Muthukumar, M. "Pattern formation in drying droplets of polyelectrolyte and salt." *The Journal of Chemical Physics* 133.11 (2010): 114905.

[27] Harrington, G. F., Campbell, J. M., & Christenson, H. K. "Crystal patterns created by rupture of a thin film." *Crystal Growth & Design* 13.11 (2013): 5062-5067.

[28] Sefiane, K. "Patterns from drying drops." *Advances in Colloid and Interface Science* 206 (2014): 372-381.

[29] Parsa, M., Harmand, S., & Sefiane, K. "Mechanisms of pattern formation from dried sessile drops." *Advances in Colloid and Interface Science* 254(2018): 22-47.

[30] Misyura, S. Y. "Heat transfer of aqueous salt solution layers." *International Journal of Heat and Mass Transfer* 125 (2018): 610-617.

[31] Wang, Z., Orejon, D., Sefiane, K., & Takata, Y. “Water vapor uptake into hygroscopic lithium bromide desiccant droplets: Mechanisms of droplet growth and spreading.” *Physical Chemistry Chemical Physics* (2018). (DOI: 10.1039/c8cp04504f)

[32] Batchelor, G. K. *An introduction to fluid dynamics*. Cambridge University press: Cambridge, 2000.

[33] Orejon, D., Sefiane, K., & Shanahan, M. E. R. “Stick–Slip of Evaporating Droplets: Substrate Hydrophobicity and Nanoparticle Concentration.” *Langmuir* 27.21 (2011): 12834-12843.

[34] Nguyen, T. A., Hampton, M. A., & Nguyen, A. V. "Evaporation of nanoparticle droplets on smooth hydrophobic surfaces: the inner coffee ring deposits." *The Journal of Physical Chemistry C* 117.9 (2013): 4707-4716.

[35] Kim, J. H., Ahn, S. I., Kim, J. H., & Zin, W. C. "Evaporation of water droplets on polymer

520 surfaces." *Langmuir* 23.11 (2007): 6163-6169.

521 [36] Bhardwaj, R., Fang, X., Somasundaran, P., & Attinger, D. "Self-assembly of colloidal particles from
522 evaporating droplets: role of DLVO interactions and proposition of a phase diagram." *Langmuir* 26.11
523 (2010): 7833-7842.

524 [37] Pan, Z., Dash, S., Weibel, J. A., & Garimella, S. V. "Assessment of water droplet evaporation mechanisms
525 on hydrophobic and superhydrophobic substrates." *Langmuir* 29.51 (2013): 15831-15841.

526 [38] Dunn, G. J., Wilson, S. K., Duffy, B. R., David, S., & Sefiane, K. "The strong influence of substrate
527 conductivity on droplet evaporation." *Journal of Fluid Mechanics* 623 (2009): 329-351.

528 [39] Ristenpart, W. D., Kim, P. G., Domingues, C., Wang, J., & Stone, H. A. "Influence of substrate
529 conductivity on circulation reversal in evaporating drops." *Physical Review Letters* 99 (2007): 234502.

530 [40] Xu, X., & Luo, J. "Marangoni flow in an evaporating water droplet." *Applied Physics Letters* 91.12 (2007):
531 124102.

532 [41] Xu, X., Luo, J., & Guo, D. "Criterion for reversal of thermal Marangoni flow in drying drops." *Langmuir*
533 26.3 (2009): 1918-1922.

534 [42] Cussler, E. L. *Diffusion: mass transfer in fluid systems*. Cambridge University press: Cambridge 3rd Edition,
535 2009.

536 [43] Dill, K., & Bromberg, S. *Molecular driving forces: statistical thermodynamics in biology, chemistry,*
537 *physics, and nanoscience*. Garland Science: New York 2nd Edition, 2010.

538 [44] Patek, J., & Klomfar, J. "A computationally effective formulation of the thermodynamic properties of
539 LiBr–H2O solutions from 273 to 500 K over full composition range." *International Journal of*
540 *Refrigeration* 29.4 (2006): 566-578.